Estimating the accuracy of a reduced-order model for the calculation of fractional flow reserve (FFR)

Etienne Boileau[1], Sanjay Pant[1], Carl Roobottom[2], Igor Sazonov[1], Jingjing Deng[3], Xianghua Xie[3], Perumal Nithiarasu[1*†]

[1] *Zienkiewicz Centre for Computational Engineering, Engineering Central, College of Engineering, Swansea University Bay Campus, Swansea, SA1 8EN, UK*

[2] *Derriford Hospital and Peninsula Medical School Plymouth Hospitals NHS Trust*

[3] *Department of Computer Science, Swansea University, Swansea SA2 8PP, UK*

SUMMARY

Image-based non-invasive fractional flow reserve (FFR) is an emergent approach to determine the functional relevance of coronary stenoses. The present work aimed to determine the feasibility of using a method based on coronary computed tomography angiography (CCTA) and reduced-order models (0D-1D) for the evaluation of coronary stenoses. The reduced-order methodology ($cFFR_{RO}$) was kept as simple as possible and did not include pressure drop or stenosis models. The geometry definition was incorporated into the physical model used to solve coronary flow and pressure. $cFFR_{RO}$ was assessed on a virtual cohort of 30 coronary artery stenoses in 25 vessels and compared with a standard approach based on 3D computational fluid dynamics ($cFFR_{3D}$). In this proof-of-concept study, we sought to investigate the influence of geometry and boundary conditions on the agreement between both methods. Performance on a per-vessel level showed a good correlation between both methods (Pearson's product-moment R = 0.885, P ¡ 0.01), when using $cFFR_{3D}$ as the reference standard. The 95% limits of agreement were -0.116 and 0.08, and the mean bias was -0.018 (SD =0.05). Our results suggest no appreciable difference between $cFFR_{RO}$ and $cFFR_{3D}$with respect to lesion length and/or aspect ratio. At a fixed aspect ratio, however, stenosis severity and shape appeared to be the most critical factors accounting for differences in both methods. Despite the assumptions inherent to the 1D formulation, asymmetry did not seem to affect the agreement. The choice of boundary conditions is critical in obtaining a functionally significant drop in pressure. Our initial data suggest that this approach may be part of a broader risk assessment strategy aimed at increasing the diagnostic yield of cardiac catheterisation for in-hospital evaluation of hæmodynamically significant stenoses.

*Correspondence to: Perumal Nithiarasu, Zienkiewicz Centre for Computational Engineering, Engineering Central, College of Engineering, Swansea University Bay Campus, Swansea, SA1 8EN, UK

This article has been accepted for publication and undergone full peer review but has not been through the copyediting, typesetting, pagination and proofreading process, which may lead to differences between this version and the Version of Record. Please cite this article as Int. J. Numer. Meth. Biomed. Engng., e02908. doi: 10.1002/cnm.2908

Received . . .

KEY WORDS: Non-invasive fractional flow reserve; reduced-order model; coronary stenosis severity, shape and asymmetry; boundary conditions

1. INTRODUCTION

Fractional flow reserve (FFR) is the current standard of care for the physiologic assessment of coronary artery stenoses [1, 2]. According to the 2014 ESC/EACTS (European Society of Cardiology/European Association for Cardio-Thoracic Surgery) Guidelines on myocardial revascularisation, when functional information is lacking, FFR has a Class I Level A recommendation to identify hæmodynamically relevant lesions in patient with stable coronary artery disease (CAD), *i.e.* data from multiple randomised trials or meta-analyses have shown that FFR is beneficial and effective [3]. Compared with anatomically complete revascularisation by percutaneous coronary intervention (PCI) based on quantitative coronary angiography (QCA), an FFR-guided strategy avoids unnecessary stenting, improves overall health outcomes, and is cost-saving [4, 5, 6, 7, 8]. In patients with multi-vessel disease, the 2014 ESC/EACTS Guidelines assign a Class IIa Level B recommendation for an FFR-guided PCI [9]. Despite the weight of evidence in favour of its usefulness, the usage of FFR appears to be under-reported [10]. In the United Kingdom, less than 10% of PCI procedures in 2010 employed FFR to guide management (in [11]). The reasons for this low adoption rate are unclear, but the invasive nature of the operation may hinder the application of FFR in practice, compared with non-invasive functional testing. Fractional flow reserve also requires conditions of maximal hyperæmia, or minimal micro-circulatory resistance, such that a linear pressure-flow relation can be assumed to be valid [12, 13]. There are alternative methods that do not rely on the concept of maximal hyperæmia, such as the instantaneous wave-free ratio (iFR) [14] or the fractional myocardial mass (FMM) [15], but *non-invasive FFR* has drawn a lot of attention as a means of 'triaging' patients and informing the choice of appropriate diagnostic investigations. In the last 5 years only, several methods have been put forward to estimate FFR with minimally invasive procedures, generally from coronary angiography or from coronary computed tomography angiography (CCTA) imaging data. In most applications, a patient-specific geometrical model is created using semi-automatic algorithms for coronary segmentation. Additional information based on form and function relationships is then added to the physiological model which complements the physical model used to solve coronary flow and pressure. In practice,

†E-mail: p.nithiarasu@swansea.ac.uk

a major part of the physiological model is also based on the imaging data. In the rest of this paper, we refer to a generic non-invasive FFR methodology as $cFFR_{img}$[†].

1.1. Non-invasive FFR

Approaches to $cFFR_{img}$ can be broadly classified according to *(i)* the 'computational methodology' underpinning the physical model, whether it involves three-dimensional (3D) or simplified models or else according to *(ii)* the physiological model, *i.e.* the boundary conditions, often represented as 0D or lumped models for the heart, the coronary and systemic circulations. Three-dimensional modelling is computationally more expensive, typically requiring off-site supercomputer analysis [16, 17, 18], but is generally considered to be more accurate. Other approaches based on 3D models include the work of [11, 19, 20, 21, 22]. Methodologies based on reduced-order or 1D models typically solve for a single axial component of velocity, area and/or pressure with an assumed profile function and require the use of empirical pressure loss formulations [23], or else are combined with 3D models. These include the work of [24, 25, 26, 27, 28, 29, 30, 31].

Unsurprisingly, a critical component of $cFFR_{img}$ is the physiological model which should be able to replicate the coronary flow and pressure during maximal hyperæmia. For both the 3D and reduced-order approaches to non-invasive FFR, adenosine administration is not required during imaging, which is generally performed under resting conditions. A key assumption is that the increase in flow, under hyperæmic conditions, is proportional to the resting flow, such that total coronary resistance at maximal hyperæmia is a fraction of its resting value [32]. Appropriate boundary conditions thus need to be specified at the inlet and, particularly, at the outlet(s), using for instance a 'coronary lumped model' [33].

One of the major unknowns in anatomical measurements is micro-circulatory resistance. Since FFR is based on average quantities (mean arterial pressure), a good estimation of resistance is critical. This can be done using flow-diameter relationships such as Murray's law, because the calibre of blood vessels adapt proportionally to flow. Consequently, in the computational model, setting the resistance distal to a stenosis will depend on the number and size of vessels downstream. In practice, several methods have been used to determine the flow distribution, depending on the number of branches included in the geometrical model. One can distribute flow based on the reference vessel or proximal segments, assuming that the feeding territory of a branch is related to its calibre before narrowing [34, 20, 30], or else based on the downstream vascular anatomy [35, 36]. A majority of

[†] FFR_{CT}, CT-based FFR, CTA- or CT-FFR, cFFR; FFR_{angio}, FFR_{QCA} or vFFR all refer to non-invasive or minimally invasive methodologies based on CCTA or angiography imaging data, respectively. cFFR stands for computed FFR; vFFR for virtual FFR.

studies rely on the fact that micro-circulatory resistance does not change with epicardial stenosis severity, however this will only be true if collateral flow is properly taken into account [37], which is generally not possible. Until collateral flow develops, admittedly, the feeding territory of a branch may not change; but the estimated resistance will still depend on whether major side branches are included or not (see *e.g.* [19], who used uniform flow in a single branch).

When $cFFR_{img}$ is derived from CCTA, it is also possible to extract additional information from the imaging data, such as myocardial volume, which can then be used to derive total coronary flow at rest. Typically, the technique only requires one acquisition phase, but if using 4-phase CT, calculation of structural data may provide more personalised boundary conditions [31]. Additional measurements, such as brachial pressure can be used to derive aortic pressure and incorporated into more complex heart and coronary models, see [36, 16, 17, 18] and variants [24, 26, 27, 28, 29, 30]. Other boundary condition strategies include the prescription of pressure at the inlet, coupled with Windkessel models at the outlets [11] or steady-state simulations with uniform pressure and/or flow derived from imaging data [21, 22] or else measured from 3D QCA and TIMI frame count [20].

In the present work, we demonstrate the feasibility of using CCTA imaging data and coronary flow simulations entirely based on reduced-order models to predict physiological measures such as FFR. Our approach is formulated using coupled 1D-0D models, but no assumption is made regarding a stenosis, *i.e.* there is no stenosis or pressure drop models that rely on a manual identification and characterisation of lesions. The computational domain is represented by a definition as accurate as possible of the geometry and cFFR is determined solely based on the physical model, supplemented with appropriate boundary conditions. The proof-of-concept is based on a thorough analysis and comparison between the proposed methodology, referred to as $cFFR_{RO}$, and an approach based on 3D computational fluid dynamics (CFD), referred to as $cFFR_{3D}$. Both approaches used in this paper are thus also generic $cFFR_{img}$ methodologies. We assessed the performance of our approach by analysing the effect of the following on 1D *vs.* 3D cFFR agreement: *(i)* stenosis severity, *(ii)* stenosis aspect ratio, *(iii)* stenosis shape, and *(iv)* stenosis asymmetry. Using a virtual cohort of 25 vessels, over which we had full control of the geometry including location and number of lesions per vessels, we show that $cFFR_{RO}$ correlates well with $cFFR_{3D}$ in predicting the physiological significance of coronary lesions. We also investigated the effect of using different boundary conditions on the $cFFR_{RO}$ measurements.

2. METHODOLOGY

2.1. Geometrical model

All cases used in this study were generated from a single anonymised historic CT coronary angiogram from a patient with minor stenosis in the left anterior descending artery. After segmentation of the left main coronary artery and its major branches, a reference surface mesh was generated. From the reference geometry, we then created 18 different axisymmetric and 7 non-axisymmetric artificial stenoses. The proximal reference diameter was 3mm, the mean diameter of all stenoses was 1.56+-0.48mm, and the diameter at the outlet of the stenotic branch was 1.5mm. Amongst the axisymmetric cases, *(i)* 3 include variations in diameter only, from 50%, 75% and up to 89% reduction; *(ii)* at a fixed severity of 75% reduction in diameter, 2 cases include variations in aspect ratio, defined as the ratio of stenosis length over the corresponding healthy vessel diameter; *(iii)* 6 cases with varying degree of severity and different aspect ratios include surface irregularities (stenosis shape); *(iv)* 5 cases include two sequential stenoses either with the same aspect ratio but a change in severity between the proximal and distal lesions (75% and 89% reduction in diameter and vice versa), or with the same severity (75% reduction in diameter) but a change in aspect ratio between the proximal and distal lesions; and finally, *(v)* 2 cases were created at a different location (one close to the bifurcation, the other further downstream). Amongst the non-axisymmetric cases, *(vi)* 3 include variations in diameter only, from 50%, 75% and up to 89% reduction; *(vii)* at a fixed severity of 75% reduction in diameter, 2 cases include variations in aspect ratio; and *(viii)* 2 cases with varying degree of severity (at a fixed aspect ratio) include surface irregularities. Selected cases from this virtual cohort are shown in Fig. 1.

For the 1D simulations, vessel centrelines as well as radii were extracted from the surface meshes using VMTK [38]. The 1D graph was reconstructed from the centreline information. The algorithm implemented in VMTK computes centrelines from surface models, but coronary centreline extraction could also be performed directly from the CCTA data; however this remains a challenging problem and is not the subject of this work. For the 3D simulations, the volume meshes were generated through the Meshsim software (Simmetrix Inc, NY) with approximately 800000 tetrahedral elements and five boundary layers.

2.2. Physiological model and boundary conditions

Based on the reference anatomy, we used the same boundary conditions (and the same micro-vascular functional reserve) for all the cases, prescribing a flow waveform at the inlet and coronary lumped models at the outlets. The inlet flow waveform is depicted in Fig. 4, the coronary model in

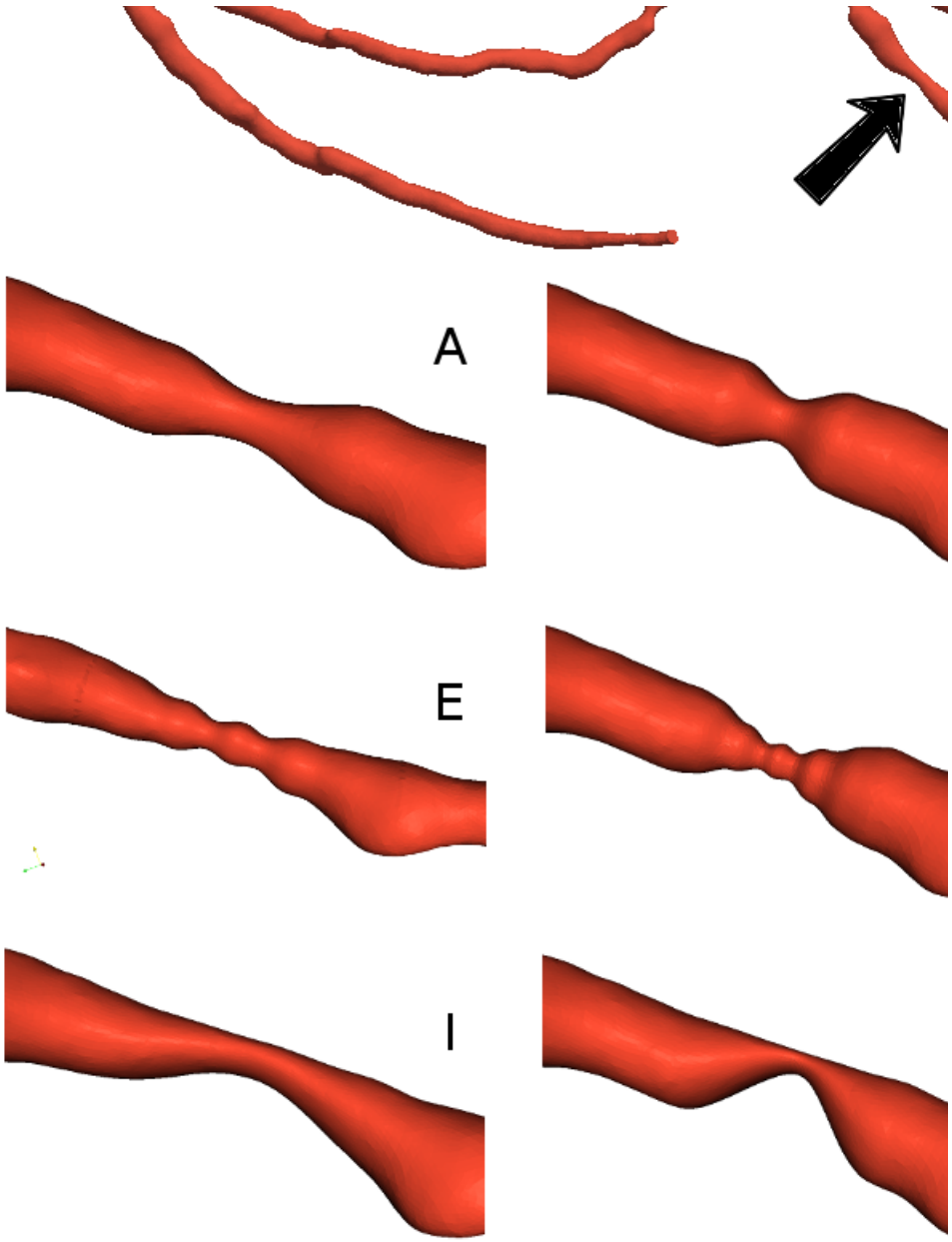

Figure 1. Selected vessels from the virtual cohort showing the reference vessel (*top left*), sequential stenoses (*top middle*), a distal stenosis (*top right*), and a close-up of different cases (A to L). Most stenoses are situated in the middle third of the vessel at the location indicated by the black arrow. Cases (A) to (F) are axisymmetric and cases (G) to (L) are non-axisymmetric. All axisymmetric stenoses shown on the image have a severity of 75% reduction in diameter, except otherwise mentioned. The baseline aspect ratio is denoted by AS. In order from left to right, top to bottom: (A) AS; (B) AS/2; (C) 2AS; (D) AS with irregular shape; (E) 2AS with irregular shape; (F) AS with irregular shape and 89% severity; (G) AS and 50% severity; (H) AS/2 and 75% severity; (I) 2AS and 75% severity; (J) AS and 89% severity; (K) AS with irregular shape and 89% severity; and finally (L) AS with irregular shape and 50% severity.

Fig. 2. For each case, we assumed that hyperæmic micro-circulatory resistance was identical to that of the reference case (no stenosis), see for instance [36]. See also [11, 19, 21] who use a 'one-size-fits-all' approach. The coronary model is adapted from previously published models [33, 35].

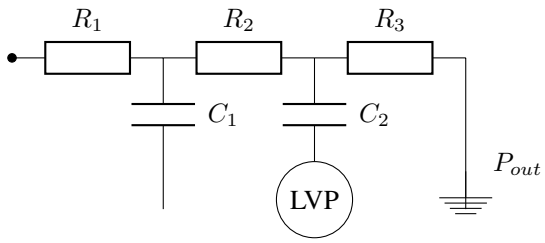

Figure 2. Lumped-parameter coronary models are coupled to the outlets of the domain to represent coronary micro-circulation. R_1 is the characteristic impedance, R_2 the micro-circulatory arterial resistance, whereas R_3 stands for micro-circulatory venous and venous resistances. C_1 is an arterial capacitance, C_2 the intra-myocardial capacitance and LVP the varying left-ventricular pressure. The coronary outflow pressure P_{out} is set to 5mmHg.

2.2.1. Choice of the parameter values for the coronary model We assumed a cardiac output of 6l min^{-1} at rest. The prescribed total mean coronary flow was 5% of the cardiac output and divided accordingly between the model (left) branch and an hypothetical right coronary artery branch in a ratio of 6:4. The details are given in Appendix A. The flow distribution to each branch was calculated on the basis of morphology data in proportion to vessel area [39]. For the 1D-3D comparison, we used proximal segments, but simulations were also performed using the downstream vascular anatomy. The results of these simulations are presented in Sect. 3.3. We assumed that myocardial demand was fixed and that baseline flow was proportional to this demand. For each coronary outlet (Fig. 2), coronary venous resistance (R3) was calculated on the basis of the mean flow to that branch and assigned venous pressure. We then computed coronary arterial resistance (R1) and coronary arterial micro-circulation resistance (R2) using branch mean flow and a target mean arterial pressure. For resting conditions, the same mean flow was obtained to all the branches as with the reference case.

The capacitance values were adjusted to give physiologically realistic coronary flow and pressure waveforms. We used 0.013ml mmHg^{-1} $100\text{g}_{\text{myo}}^{-1}$ and 0.254ml mmHg^{-1} $100\text{g}_{\text{myo}}^{-1}$ for arterial (C1) and intra-myocardial (C2) capacitance, respectively [40, 41, 42]. As the value for the capacitance (C2) originally accounts for venous compliance, we only took a proportion of this value. The capacitances were then distributed to each branch in proportion of vessel area. We assumed a total feeding territory of 120g of myocardium, *cf.* [43] for normal values of left ventricular mass, also [35] who reports a FMM in the range range75g to 103g in the left main, based on allometric scaling between length of coronary arterial tree and left ventricular myocardial mass.

Finally, we modelled the effect of intra-coronary vasodilators, such as adenosine, by reducing all the coronary resistances uniformly by a factor of 0.22, corresponding to a 3.5-fold increase in flow with respect to resting conditions [32]. As in a majority of studies, we assumed that hyperæmic conditions did not significantly affect the heart rate and blood pressure.

2.2.2. Intramyocardial pressure Flow in the left coronary arteries is predominantly diastolic. This phenomenon is partly explained by the concept of intra-myocardial or cavity-induced extracellular pressure. In our model, we used a prescribed left ventricular pressure waveform (LVP in Fig. 2, see also Fig. 4), as we did not have a heart model. The intra-myocardial pressure corresponds to a fraction of the cavity pressure for epicardial vessels, see for instance [44].

2.3. 1D model and material properties

In the 1D formulation, the coronary arteries are decomposed into a number of segments connected to each other. Each segment is modelled as a deformable tube whose properties are described by a single axial coordinate x. The system of equations that describes blood flow is given in AU form by

$$\begin{cases} \dfrac{\partial A}{\partial t} + \dfrac{\partial (AU)}{\partial x} = 0 \\ \dfrac{\partial U}{\partial t} + U\dfrac{\partial U}{\partial x} + \dfrac{1}{\rho}\dfrac{\partial P}{\partial x} = \dfrac{f}{\rho A} \end{cases} \tag{1}$$

where t is the time, $A(x,t)$, $U(x,t)$ and $P(x,t)$ are the cross-sectional average area, velocity and pressure, respectively, and ρ is the density of blood. In this work, the axial velocity profile u was given by

$$u(x,\xi,t) = U(x,t)\frac{\zeta+2}{\zeta}\left[1-\left(\frac{\xi}{R}\right)^{\zeta}\right] \tag{2}$$

where $R(x,t)$ is the vessel radius, ξ is the radial coordinate, and ζ is a given constant for a particular profile. We used ζ =9 [45]. Using Eq. (2), the frictional force in Eqs. (1) becomes $f = -2(\zeta+2)\mu\pi U$, where μ is the dynamic viscosity of blood. For both 1D and 3D simulations, the density and dynamic viscosity were ρ =1.06g cm $^{-3}$ and μ =0.04g cm^{-1} s^{-3}, respectively.

Equations (1) were solved using a standard discontinuous Galerkin (DG) formulation written in conservative form with a high-order 1D spectral/*hp* spatial discretisation. Time integration was performed explicitly using a 2$^{\text{nd}}$ order Adams-Bashforth method, subject to a CFL condition. For more details on the method and on the 1D formulation applied to blood flow simulations, the reader is referred to [46].

The geometry definition was incorporated into the finite element formulation through a reference area and expanded using the same basis function. Briefly, after extracting the centrelines, the radius distribution along each branch was used to interpolate the reference area (A_0) and material properties (β), as described below. We used Legendre polynomials, but we are not restricted by the choice of basis function. Provided that the information obtained from the radius distribution is fine enough, the fidelity and exactness of the geometry thus only depend on the polynomial order and the choice of quadrature.

The vessel wall was modelled as an elastic material with properties (β) estimated using the empirical relation given in [47]. The pressure-area relationship or 'tube law' was based on Laplace's law

$$P - P_{ext} = P_0 + \frac{\beta}{A_0}\left(\sqrt{A} - \sqrt{A_0}\right) \tag{3}$$

$$\beta = \frac{4}{3}\sqrt{\pi}Eh \tag{4}$$

$$Eh = R_0\left(k_1 e^{k_2 R_0} + k_3\right) \tag{5}$$

where P_{ext} =0mmHg is the external pressure; P_0 =80mmHg is the reference or diastolic pressure; R_0 and A_0 are the reference radius and cross-sectional area obtained from the CCTA imaging data, respectively; and where k_1 =2e7g^2 s^{-1} cm^{-1}, k_2 =-22.53cm^{-1} and k_3 =8.65e5g^2 s^{-1} cm^{-1}. This type of tube law has been used extensively, see [46] and references therein.

2.4. 3D rigid model

The 3D simulations were run using the streamline upwind Petrov Galerkin (SUPG) finite-element solver [48] for incompressible Navier-Stokes equations made available in the Simvascular project [49]. For the inlet, a Womersley velocity profile was imposed, and at the outlets the lumped-parameter coronary model depicted in Fig. 2 was imposed through a user subroutine. An implicit coupling between the lumped-parameter model and the 3D boundaries was employed [50].

3. RESULTS

A non-invasive cFFR measurement was obtained by normalising the mean hyperæmic distal pressure by the mean hyperæmic pressure at the most proximal section of the stenosed branch. To compare cFFR_{RO} with cFFR_{3D}, we selected a number of points along the centreline and their corresponding planes in the 3D model, where the spatial averages were calculated (Fig. 3). Additionally, for visual assessment, at any given point in the coronary vessels, cFFR was computed by taking the ratio of the average of the local pressure to the average proximal or aortic pressure. In the case of sequential stenoses (where cFFR was computed per-lesion), we used the formula given in [51] to predict FFR for each stenosis separately, assuming that coronary occlusive pressure was P_w = 0. We note that even in the absence of collaterals, as in this case, a distal stenosis will influence the hæmodynamics of a proximal lesion, and thus also its predicted cFFR.

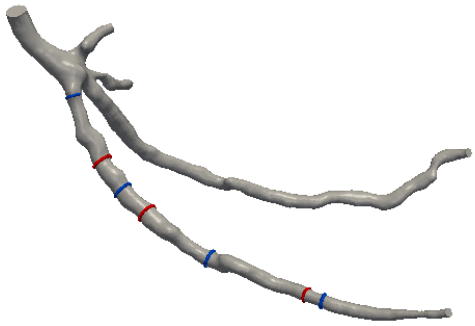

Figure 3. Cross-sectional planes along the stenosed branch in the 3D model. The location of different stenosis cases are highlighted in red. For the 1D-3D cFFR comparison, measurements were taken at locations indicated in blue. The first plane in blue towards the bifurcation corresponds to the proximal or aortic pressure P_a. Other planes in blue indicate the location of the distal pressure (P_d) measurements for different cases. The computed fractional flow reserve is given by cFFR = P_d/P_a, in the case of a single stenosis, or when computed on a per-vessel basis. To predict cFFR for each stenosis separately, in the case of sequential stenoses, we used the formula given in [51].

3.1. Comparison between 1D and 3D results

We show in Fig. 4 a comparison between 1D and 3D results for the reference geometry, a typical case of agreement and the worst case of agreement. The former is a non-axisymmetric stenosis with 89% severity and baseline aspect ratio, shown in Fig. 1 (J); the latter is an irregular shaped axisymmetric stenosis with 89% severity and baseline aspect ratio, shown in Fig. 1 (F).

We also show a comparison of cFFR for these two cases in Fig. 5. Discrepancies between these cases are discussed in more details in Sect. 4.

3.2. Comparison between $cFFR_{RO}$ and $cFFR_{3D}$

The mean systolic and diastolic aortic pressure was 123.9+-1.1mmHg and 73.6+-1.0mmHg, respectively, for the 1D simulations, and 122.6+-1.6mmHg and 69.8+-1.7mmHg, respectively, for the 3D simulations. Comparison of $cFFR_{3D}$ and $cFFR_{RO}$ was performed in 30 coronary artery stenoses on 25 vessels from our virtual cohort. Approximately 13% of the stenoses had a severity of 50% reduction in diameter, 67% had a severity of 75%, and 20% had a severity of 89%, thus most cases were intermediate-to-significant stenoses. The mean cFFR computed with the 3D model was 0.89+-0.09, and that computed with the 1D model was 0.90+-0.06. The overall correlation between $cFFR_{3D}$ and $cFFR_{RO}$ was very good (Pearson's product-moment R = 0.885, P ¡ 0.01, Fig. 6). The agreement between $cFFR_{3D}$ and $cFFR_{RO}$ became less accurate with positive (¡ 0.80) measurements, but with no significant bias (Fig. 7).

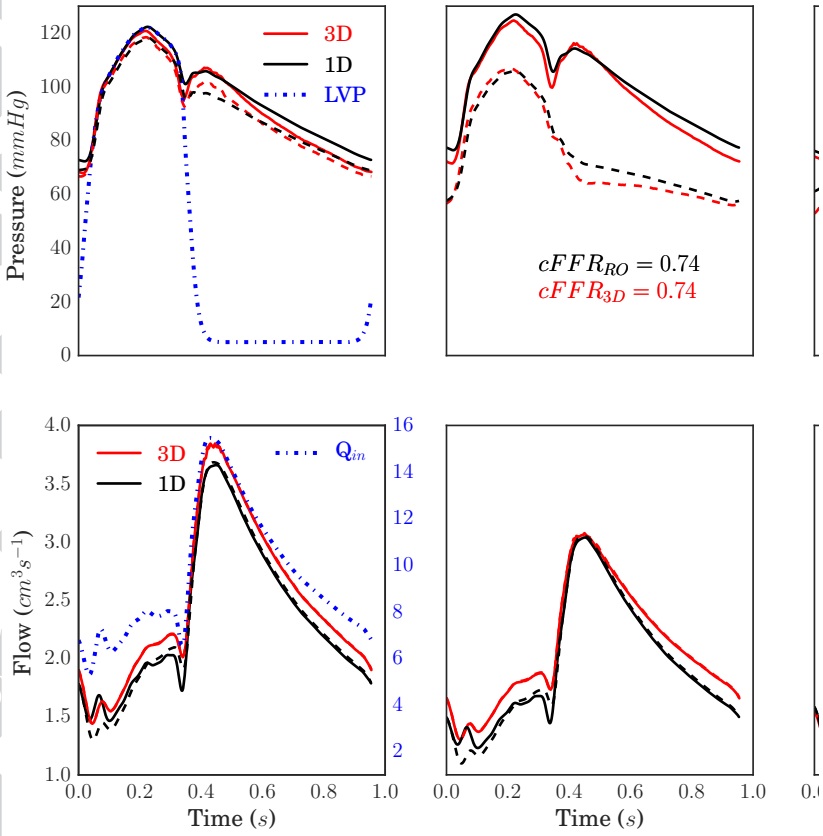

Figure 4. Comparison between 1D and 3D results. Pressure is shown on the top (the solid line is P_a, the broken line is P_d) and flow rate on the bottom. From left to right: *(i)* reference geometry, *(ii)* a typical case of agreement with a severe stenosis (Fig. 1 J), and *(iii)* the worst case of agreement with a severe stenosis (Fig. 1 F). The left ventricular pressure (LVP) used in the coronary model is shown in blue *(top left)*. The inlet flow waveform is shown in blue *(bottom left)*.

At a threshold of 0.80, 7 lesions were hæmodynamically significant when using $cFFR_{3D}$ as a reference standard; 3 of these were classified by both $cFFR_{RO}$ and $cFFR_{3D}$ as relevant, whereas $cFFR_{RO}$ classified the remaining 4 lesions as non-significant. A total of 23 stenoses were classified by both as non-significant.

3.3. Influence of the geometry and boundary conditions on $cFFR_{RO}$

Comparison of $cFFR_{3D}$ and $cFFR_{RO}$ was performed in 30 coronary artery stenoses and further classified non-exclusively into *(i)* stenoses of varying severity and shapes at a fixed aspect ratio (baseline); *(ii)* stenoses of varying aspect ratio and shapes at a fixed severity of 75%; and finally *(iii)* stenoses with surface irregularities only. These results are shown in Fig. 8. There was no apparent discrepancies between axisymmetric (2 stenoses had a severity of 50%, 17 had a severity of 75% and

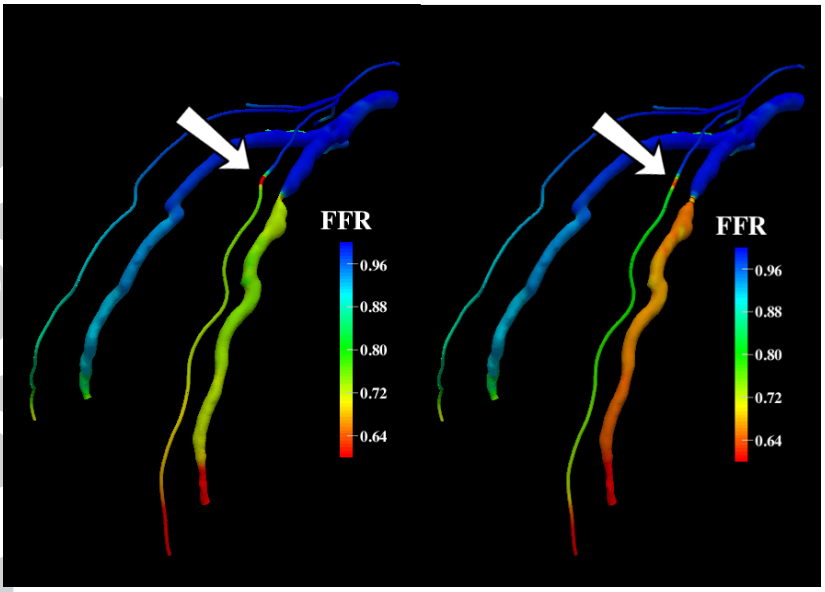

Figure 5. Comparison between $cFFR_{RO}$ and $cFFR_{3D}$ for *(left)* a typical case of agreement ($cFFR_{RO}$ = $cFFR_{3D}$ =0.74), and *(right)* the worst case of agreement ($cFFR_{RO}$ =0.80, $cFFR_{3D}$ =0.67). Refer to Fig. 4 for more details. cFFR is displayed using a colour-coded representation for visual assessment. The stenosis is indicated by the arrow.

4 had a severity of 89%) and non-axisymmetric (2 stenoses had a severity of 50%, 3 had a severity of 75% and 2 had a severity of 89%) stenoses, but $cFFR_{RO}$ under-estimated $cFFR_{3D}$ in a majority of non-axisymmetric cases. At a fixed aspect ratio, stenosis severity (combined with stenosis shape or surface irregularities) appeared to be the most critical factor accounting for differences in cFFR estimates between both methods, with $cFFR_{RO}$ significantly over-estimating $cFFR_{3D}$ in 5 cases (2 cases with surface irregularities). Stenosis length and/or aspect ratio did not seem to influence the agreement between both methods.

We also investigated the effect of varying boundary conditions on $cFFR_{RO}$ (Fig. 9). We assumed that the current boundary conditions were correct (*i.e.* chosen such that maximal hyperæmia was achieved for a given vessel with a set of morphometric measurements accounting for unknown quantities), and used $cFFR_{RO}$ as a measure for comparison. We then re-computed cFFR for each stenoses with a different set of boundary conditions, with values of resistances being determined on the basis of the distal anatomy (outlet surfaces). The new cFFR was denoted as $cFFR^{*}_{RO}$. As expected, $cFFR_{RO}$ and $cFFR^{*}_{RO}$ showed a very high correlation, however $cFFR^{*}_{RO}$ systematically over-estimated $cFFR_{RO}$, and the bias increased with values approaching or exceeding the positive threshold (¡ 0.80). The influence of the geometry and boundary conditions on $cFFR_{RO}$ is discussed in more detail below.

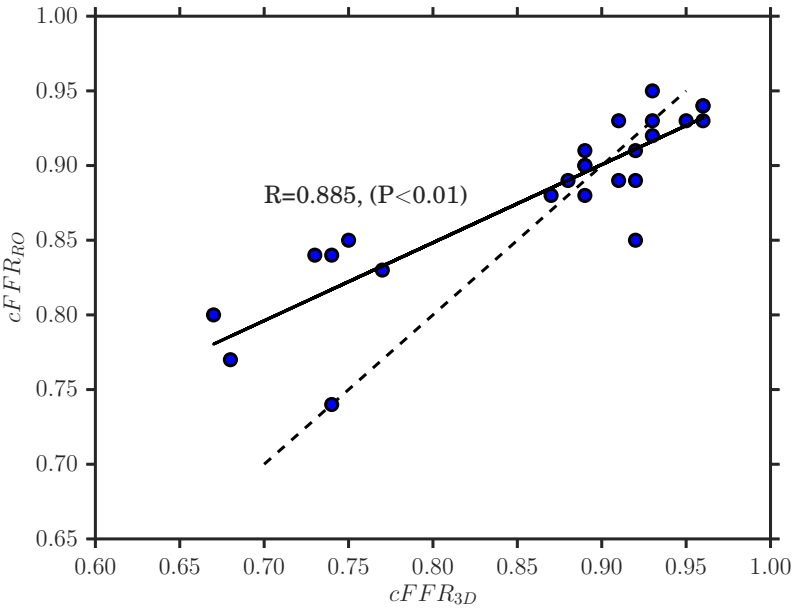

Figure 6. Performance on a per-vessel level for the identification of stenoses demonstrates a good correlation between $cFFR_{RO}$ and $cFFR_{3D}$, when using $cFFR_{3D}$ as a reference standard (Pearson's product-moment R = 0.885, P ¡ 0.01). The line of equality is also shown (broken line).

4. DISCUSSION

A variety of non-invasive methodologies have been proposed in the last five years with the aim of providing on-site availability of $cFFR_{img}$ evaluation within a clinically viable time frame at a reasonable cost. In this study, we examined the performance of a method entirely based on coupled reduced-order (1D-0D) models for the computation of FFR from CCTA imaging data, referred to as $cFFR_{RO}$. The comparison is made with a standard methodology using CFD and 3D models, referred to as $cFFR_{3D}$, on a virtual cohort of 30 stenoses in 25 vessels. This also enabled us to

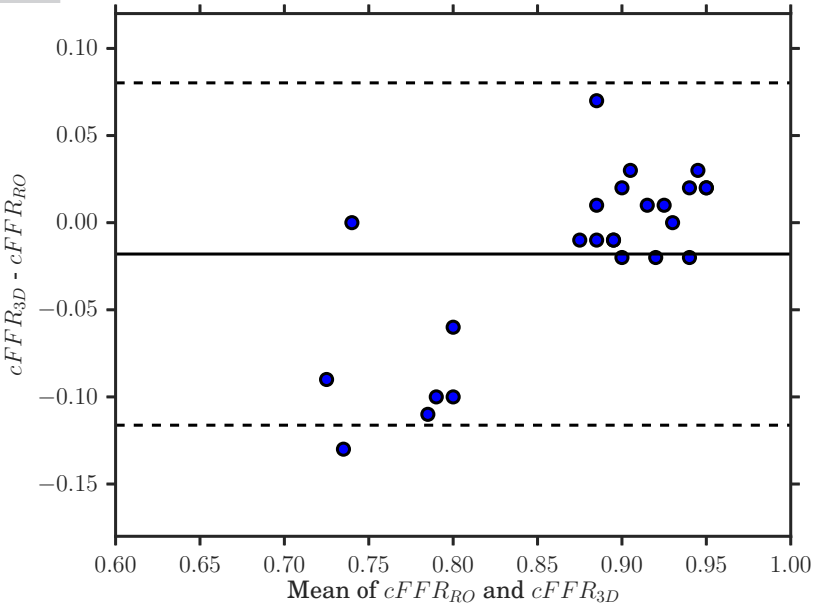

Figure 7. Bland-Altman plot comparing $cFFR_{RO}$ and $cFFR_{3D}$ on a per-vessel level shows a good agreement between the methods (95% limits of agreement -0.116 to 0.08). The mean bias was -0.018 (SD =0.05).

investigate computationally the effect of the geometry (geometrical model) and boundary conditions (physiological model) on the accuracy of the computed FFR, denoted as cFFR.

The performance of the presently studied approach remains relatively good, when compared with results from a standard $cFFR_{3D}$ methodology, regardless of the fact that we did not use a stenosis model. The pressure loss and hence $cFFR_{RO}$ is largely determined by the viscous term in the equations underpinning the physical model used in the 1D simulations. In this work, we used an approximation of a flat profile with boundary layer [45], however better approximations such as that suggested in [23] would be expected to improve the accuracy of the results. The use of a different tube law Eq. (3) may also influence the agreement between both methods, although for the

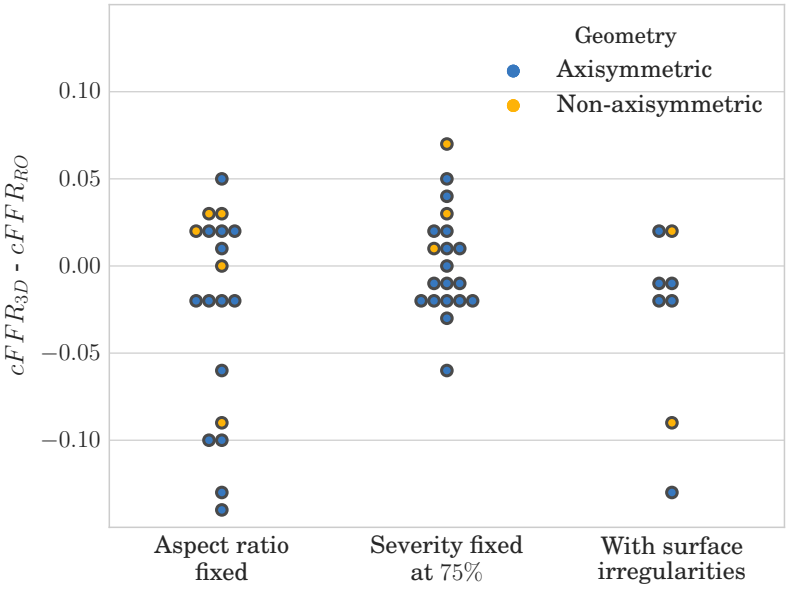

Figure 8. Error in $cFFR_{RO}$ when using $cFFR_{3D}$ as the reference standard, on a per-lesion level, for stenoses classified non-exclusively into *(i)* stenoses of varying severity and shape at a fixed aspect ratio (baseline); *(ii)* stenoses of varying aspect ratio and shape at a fixed severity of 75%; and *(iii)* stenoses with surface irregularities only; for both axisymmetric and non-axisymmetric cases.

intended application presented here, it is unclear if a more complex formulation would add additional information, given the lack of and/or the variability in structural data for human coronary arteries.

Our preliminary data demonstrated a good correlation with $cFFR_{3D}$ (Pearson's correlation coefficient R =0.885, statistically significant, Fig. 6) and generally compares favourably to the results of other studies; even if, for obvious reasons, we cannot make a fair comparison with these previously published trials. The agreement between $cFFR_{3D}$ and $cFFR_{RO}$ did not show significant bias (-0.018, SD =0.05), but became less accurate with positive (¡ 0.80) measurements (Fig. 7). In fact, the limits of agreement would become larger with positive FFR results if determined from a regression of absolute differences. This has also been observed in a majority of studies, see for

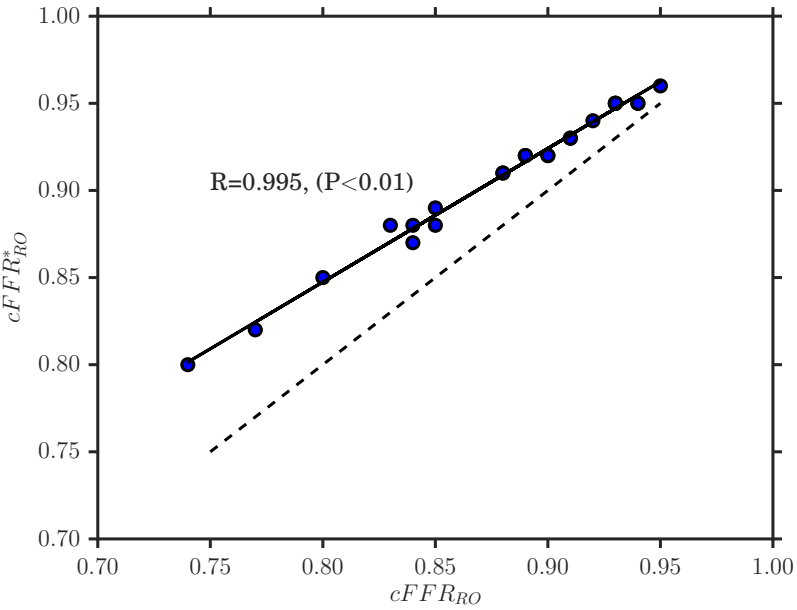

Figure 9. Scatter plot of cFFR computed on a per-vessel level with two different set of boundary conditions. $cFFR_{RO}$ is the current method, where resistances are determined on the basis of the proximal anatomy; $cFFR^*_{RO}$ is an alternative method, where resistances are determined on the basis of the distal anatomy. Both methods produced the same result in 9 cases, however $cFFR^*_{RO}$ systematically over-estimated $cFFR_{RO}$, and the bias increased with values approaching or exceeding the positive threshold (¡ 0.80). The line of equality is also shown (broken line).

instance [16, 11, 24, 19, 27]. $cFFR_{RO}$ appeared to over-estimate $cFFR_{3D}$ for the most severe lesions, thus the 1D model may not be able to capture the loss in pressure for these cases, particularly when severity is combined with an irregular shape. All 5 cases (including one outlier) shown in Fig. 7 close to the lower limit of agreement were the most severe stenoses (89% reduction in diameter), including irregular, non-axisymmetric and sequential lesions. The addition of pressure drop models may enhance the accuracy, however this requires the identification and characterisation of the lesion(s); and besides is not a guarantee of a better agreement, see *e.g.* [26, 31]. Therefore, our

results suggest that the reduced-order model presented in this study may be capable of streamlining CAD patient management.

Influence of the geometry One of the aims of this study was to assess the performance of $cFFR_{RO}$ to estimate FFR from CCTA imaging data by analysing the effect of different geometrical configurations when compared with $cFFR_{3D}$ as a reference standard. The different geometries were chosen to represent typical cases of irregular, short or long lesions, with a low or high calcium score and various degrees of severity. Selected cases are shown in Fig. 1. Three-dimensional modelling is generally considered to be more accurate, when compared with 1D models that solve for a single axial component of velocity, area and/or pressure with an assumed profile function. In the context of non-invasive FFR, it is unclear how these discrepancies, if any, will affect the accuracy of $cFFR_{RO}$. We thus chose to reduce the complexity of the 1D model at a minimum to asses the effect of the geometry on the agreement between $cFFR_{RO}$ and $cFFR_{3D}$. We classified non-exclusively the 30 cases and their corresponding $cFFR_{RO}$ measurements into 3 different groups, based on geometrical features and further differentiated into axi- and non-axisymmetric stenoses, as shown in Fig. 8. Despite the assumptions inherent to the 1D formulation, asymmetry did not seem to affect the agreement between both methods in any particular way. In fact, $cFFR_{RO}$ appeared to under-estimate $cFFR_{3D}$ in a majority of non-axisymmetric cases, even if the proportion of stenoses of intermediate-to-significant severity is slightly lower, and that of more severe stenoses is higher, in the non-axisymmetric group, when compared with the group of axisymmetric cases (72% *vs.* 83% for stenoses of intermediate severity, and 28% *vs.* 17% for severe stenoses with 89% reduction in diameter). The point shown in Fig. 6 on the line of equality is also a non-axisymmetric lesion (*cf.* Fig. 1 J and Fig. 4). We note that, for non-axisymmetric cases, the actual minimal cross-sectional area across the stenosis may be greater in 3D than that calculated in the 1D formulation, determined from the vessel radius using the maximum inscribed sphere [38], which may partly explain these observations. We are led to believe that, for clinical applications, these results would show a better agreement. Admittedly, the number of non-axisymmetric cases was significantly lower than that of axisymmetric cases (18 *vs.* 7). Even if lesion length, and more generally aspect ratio, were shown to have a physiologically significant impact on intermediate coronary stenoses [52], our results suggest no appreciable difference between $cFFR_{RO}$ and $cFFR_{3D}$. As shown in Fig. 8, at a fixed severity of 75%, but with varying aspect ratio and shape, there was no apparent bias between the two methods. At a fixed aspect ratio, however, stenosis severity appeared to be the most critical factor accounting for differences in cFFR estimates between both methods. Shape irregularity did not have a pronounced effect on the accuracy of the results, except when combined with lesion severity. For these cases and, more generally, for the largest reductions in diameter, flow separation may

occur distal to the stenosis, particularly in the laminar regime, which may result in non-negligible friction losses. Thus without further improvements, the 1D formulation would tend to predict a non-significant FFR, whereas the lesion is hæmodynamically significant. Yet, 3 out of 7 significant lesions were correctly classified ($cFFR_{RO}$ ¡ 0.80), in spite of a poor agreement. If this deserves further investigation, these limitations remain somewhat academic, as stenoses above 90% severity would not normally pose a diagnostic problem. Clinical guidelines currently recommend FFR for lesions between range5090% severity [3].

Influence of boundary conditions Irrespective of the geometry, if we assume that coronary and myocardial flow are equal and that the contribution of collateral flow is negligible, which is almost always the case in modelling studies, then the pressure drop across a stenosis only depends on the antegrade flow and the downstream resistance. Consequently, in the computational model, setting the resistance distal to a stenosis and the flow distribution through the different branches is critical. Fractional flow reserve also depends on the extent of the perfusion territory subtended by the stenosed branch. A severe flow-limiting stenosis supplying viable myocardium typically yields a positive FFR; however where blood flow requirements are small the same lesion may demonstrate a normal FFR [53]. If these considerations are factored into the estimation of boundary conditions, this also points out to another important aspect of the physiological model, which depends on the geometry, the number and size of vessels included in the reconstruction of the actual coronary physiology, and whether these are supplying the same territory. The resistance offered by these vessels may have a non-negligible impact on the flow distribution, as flow through one branch will depend not only on the resistance of that branch, but more generally on the total resistance of the tree.

In this study, resistances were determined based on the reference vessel in proportion of area [39]. As we imposed flow at the inlet, this was also equivalent to assuming a given flow distribution. Our choice was based on the assumption that the feeding territory of a branch is related to its calibre before narrowing [34, 20, 30], and that this territory will not change until collateral flow develops. To investigate the influence of assuming a different functional reserve and flow distribution to each branch, we re-computed cFFR for each stenoses with a different set of boundary conditions, where resistances were determined on the basis of the downstream vascular anatomy. We then compared $cFFR_{RO}$ with the new cFFR, denoted as $cFFR^*_{RO}$. Bland-Altmann analysis revealed an average bias of -0.029 (SD =0.013). In 15 cases of intermediate-to-significant stenoses, both methods agreed perfectly ($cFFR_{RO}$ ¿ 0.88); the agreement was still reasonable when $cFFR_{RO}$ was above 0.84; however $cFFR^*_{RO}$ systematically over-estimated $cFFR_{RO}$ below this value (Fig. 9). The results revealed a significant trend towards over-estimation as the average decreased; *i.e.* as lesions became

more significant, the discrepancies between both methods also became more apparent. Therefore, in the most severe cases, flow through the stenotic vessel was not sufficient to cause the expected drop in pressure; indeed the resistance of that branch was much higher when determined from the downstream anatomy, when compared with smaller branches of the model. This is because the physiological model is to a large extent based on the morphology, which is extracted from the geometrical model. However the critical aspect of determining boundary conditions does not seem to be that of 'personalisation', *i.e.* the inclusion of patient information such as arterial pressure or coronary structural information, as much as that of making sure that the geometrical model is consistent with the underlying assumptions of the physiological model. It is consequently crucial to accurately determine the correct hyperæmic micro-vascular resistance of each outlet. If we assume a normal vasodilatory capacity and no micro-vascular dysfunction, ultimately, if enough flow is going through the model stenosis, one may expect to recover a functionally significant drop in pressure that would yield a reasonable agreement with the measured FFR. To some extent, this would also agree with [11] and others, who used a 'universal' boundary condition strategy, and claimed that anatomical data alone would be enough to reliably predict the physiological significance of coronary lesions.

Limitations These preliminary investigations should be interpreted in view of several limitations, foremost the nature of the comparison in a small cohort which was made using $cFFR_{3D}$ as a reference standard. For this reason, we did not assess the overall indices of diagnostic accuracy for our proposed method. On the other hand, as boundary conditions were fixed, and we had full control of the geometry, this enabled us to analyse the influence of the latter on the agreement between $cFFR_{RO}$ and $cFFR_{3D}$. A number of previously published results from retrospective trials also were limited by small sample size and selection bias based on the availability of invasive FFR measurements. The framework presented in this paper has been reduced to a minimum, however the addition of more complex heart, coronary and/or systemic circulation models is not expected to change these results. A better approximation of the velocity profile function and the inclusion of pressure drop models may however improve the accuracy of $cFFR_{RO}$.

5. CONCLUSION

In this preliminary study, we assessed the feasibility of using a reduced-order method, $cFFR_{RO}$, based on CCTA for the evaluation of potentially ischæmia-causing coronary stenoses. $cFFR_{RO}$ was assessed on a virtual cohort of 30 coronary artery stenoses in 25 vessels and compared with a

standard approach based on 3D computational fluid dynamics. Performance on a per-vessel level showed a good correlation between both methods with no significant bias. Despite the assumptions inherent to the 1D formulation, asymmetry did not seem to affect the agreement; however, stenosis severity and shape appeared to be the most critical factors accounting for differences in both methods. Whether or not a simpler and faster approach to non-invasive FFR can give valuable results depends on how well the pressure drop can be predicted, and thus the determination of boundary conditions is critical. In future studies, the clinical relevance of the current findings should be assessed and compared with invasive coronary catheter angiography-based measurement of FFR.

ACKNOWLEDGEMENTS

This project is partly funded by the Life Sciences Bridging Fund (LSBF/R6-002). The authors would like to thank HPC Wales (www.hpcwales.co.uk) for providing the high performance computing facilities. The authors would also like to acknowledge the contribution of Rob Alcock (Plymouth Hospitals NHS Trust), Jonathan Mynard (Murdoch Childrens Research Institute), Kevin Mohee and Daniel Rhys Obaid (Abertawe Bro Morgannwg University Health Board NHS Trust).

A. ESTIMATION OF BOUNDARY CONDITIONS

The procedure described below was used to estimate the boundary conditions from morphology, either according to the proximal or to the downstream vessel anatomy.

A.1. Estimation of boundary conditions at rest

The resistance at each outlet was determined from the ratio of the pressure to the flow through that outlet. Mean arterial pressure (MAP) was assumed to be constant and the total coronary flow at rest Q_{rest} was given as described in Sect. 2.2.1. In a general situation, pressure can be estimated from systolic/diastolic cuff pressures and heart rate, and Q_{rest} from the imaging data; but alternative strategies have been proposed which are briefly reviewed in Sect. 1.1. We used the lumped-parameter coronary model shown in Fig. 2. The boundary condition estimation is thus equivalent to determining and distribute the resistance to the various coronary models at the outlets. Based on [39], flow was distributed according to the square (and not, as in Murray's law, according to the cube) of the diameter, or in proportion of vessel area

$$Q_i \sim A_i \tag{6}$$

where A_i is the area of the vessel. As the total resting flow Q_{rest} is the sum of all outlet flows, the flow through one particular branch was determined using

$$Q_i = Q_{rest} \frac{A_i}{\sum A_j} \tag{7}$$

where $j = 1, \ldots, n$ and n is the total number of branches included in the geometrical model. The terminal resistance was given by

$$R_i = \frac{MAP}{Q_i}. \tag{8}$$

At each outlet, the terminal resistance R_i was then distributed as described in Sect 2.2.1. The venous resistance $R_{i,3}$ was determined assuming a venous pressure of 20mmHg with P_{out} =5mmHg. The arterial resistance $R_{i,1}$ was the characteristic impedance, calculated using

$$R_{i,1} = \frac{\rho c_i}{A_i} \tag{9}$$

$$c_i = \sqrt{\frac{2}{3\rho}\left(k_1 e^{k_2 R_{0,i}} + k_3\right)} \tag{10}$$

where c_i is the pulse wave velocity estimated from the reference radius $R_{0,i}$ using the empirical relation given in [47], see Sect. 2.3. Radius information was extracted from the geometry. The micro-circulatory arterial resistance $R_{i,2}$ was taken as the difference between total resistance to this branch and the sum of the characteristic impedance and venous resistances.

A.2. Estimation of boundary conditions at hyperæmia

To simulate the effect of intra-coronary vasodilators such as adenosine, we assumed that effective resistance decreased by a constant factor, referred to as the total coronary resistance index (TCRI)

$$TCRI = \frac{R_{hyperæmia}}{R_{rest}}. \tag{11}$$

Values have been reported in the range 0.22 - 0.28, see *e.g.* [54, 55]. The most often cited work is that of [32]. In this study, we used $TCRI$ =0.22, which corresponds to an increase in flow by a factor of approximately 4.5. Hyperæmic resistance is simply determined as

$$R_{i,hyperæmia} = TCRI \cdot R_{i,rest} \tag{12}$$

where $R_{i,rest}$ are the resistance values determined at rest, as explained above. The capacitance values were determined as described in Sect. 2.2.1 and then distributed following a procedure similar to that described above.

REFERENCES

1. Pijls N, De Bruyne B, Peels K, Van Der Voort P, Bonnier H, Bartunek J, Koolen J. Measurement of fractional flow reserve to assess the functional severity of coronary-artery stenoses. *N. Engl. J. Med.* 1996; **334**:1703–1708.
2. Lotfi A, Jeremias A, Fearon W, Feldman M, Mehran R, Messenger J, et al. Expert consensus statement on the use of fractional flow reserve, intravascular ultrasound, and optical coherence tomography: A consensus statement of the society of cardiovascular angiography and interventions. *Catheter Cardiovasc. Interv.* 2014; **83**:509–518.

3. Windecker S, Kolh P, Alfonso F, Collet J, Cremer J, Falk V, et al. 2014 ESC/EACTS guidelines on myocardial revascularization: The task force on myocardial revascularization of the european society of cardiology (ESC) and the european association for cardio-thoracic surgery (EACTS) developed with the special contribution of the european association of percutaneous cardiovascular interventions (EAPCI). *Eur. Heart J.* 2014; **35**:2541–2619, .
4. Pijls N, van Schaardenburgh P, Manoharan G, Boersma E, Bech J, van't Veer M, et al. Percutaneous coronary intervention of functionally nonsignificant stenosis: 5-year follow-up of the DEFER Study. *J. Am. Coll. Cardiol.* 2007; **49**:2105–2111.
5. Tonino P, De Bruyne B, Pijls N, Siebert U, Ikeno F, van't Veer M, et al. Fractional flow reserve versus angiography for guiding percutaneous coronary intervention. *N. Engl. J. Med.* 2009; **360**:213–224, .
6. Tonino P, Fearon W, De Bruyne B, Oldroyd K, Leesar M, Ver Lee P, et al. Angiographic versus functional severity of coronary artery stenoses in the FAME study fractional flow reserve versus angiography in multivessel evaluation. *J. Am. Coll. Cardiol.* 2010; **55**:2816–2821, .
7. Pijls N, Fearon W, Tonino P, Siebert U, Ikeno F, Bornschein B, et al. Fractional flow reserve versus angiography for guiding percutaneous coronary intervention in patients with multivessel coronary artery disease: 2-year follow-up of the FAME (Fractional flow reserve versus Angiography for Multivessel Evaluation) study. *J. Am. Coll. Cardiol.* 2010; **56**:177–184, .
8. Fearon W, Bornschein B, Tonino P, Gothe R, Bruyne B, Pijls N, et al. Economic evaluation of fractional flow reserve-guided percutaneous coronary intervention in patients with multivessel disease. *Circulation* 2010; **122**:2545–2550, .
9. De Bruyne B, Pijls N, Kalesan B, Barbato E, Tonino P, Piroth Z, et al. Fractional flow reserve-guided pci versus medical therapy in stable coronary disease. *N. Engl. J. Med.* 2012; **367**:991–1001, .
10. Elgendy I, Conti C, Bavry A. Fractional flow reserve: An updated review. *Clin. Cardiol.* 2014; **37**:371–380.
11. Morris P, Ryan D, Morton A, Lycett R, Lawford P, Hose D, Gunn J. Virtual fractional flow reserve from coronary angiography: modeling the significance of coronary lesions: results from the VIRTU-1 (VIRTUal Fractional Flow Reserve From Coronary Angiography) study. *JACC Cardiovasc. Interv.* 2013; **6**:149–157, .
12. Pijls N, De Bruyne B. Coronary pressure measurement and fractional flow reserve. *Heart* 1998; **80**:539–542.
13. Spaan J, Piek J, Hoffman J, Siebes M. Physiological basis of clinically used coronary hemodynamic indices. *Circulation* 2006; **113**:446–455, .
14. Sen S, Escaned J, Malik I, Mikhail G, Foale R, Mila R, et al. Development and validation of a new adenosine-independent index of stenosis severity from coronary wave-intensity analysis: results of the ADVISE (ADenosine Vasodilator Independent Stenosis Evaluation) study. *J. Am. Coll. Cardiol.* 2012; **59**:1392–1402, .
15. Kim H, Lim H, Doh J, Nam C, Shin E, Koo B, et al. Physiological severity of coronary artery stenosis depends on the amount of myocardial mass subtended by the coronary artery. *JACC Cardiovasc. Interv.* 2016; **9**:1548–1560, .
16. Koo B, Erglis A, Doh J, Daniels D, Jegere S, Kim H, et al. Diagnosis of ischemia-causing coronary stenoses by noninvasive fractional flow reserve computed from coronary computed tomographic angiograms. Results from the prospective multicenter DISCOVER-FLOW (diagnosis of ischemia-causing stenoses obtained via noninvasive fractional flow reserve) study. *J. Am. Coll. Cardiol.* 2011; **58**:1989–1997, .
17. Min J, Leipsic J, Pencina M, Berman D, Koo B, van Mieghem C, et al. Diagnostic accuracy of fractional flow reserve from anatomic CT angiography. *JAMA* 2012; **308**:1237–1245, .
18. Norgaard B, Leipsic J, Gaur S, Seneviratne S, Ko B, Ito H, et al. Diagnostic performance of noninvasive fractional flow reserve derived from coronary computed tomography angiography in suspected coronary artery disease: the NXT trial (Analysis of Coronary Blood Flow Using CT Angiography: Next Steps). *J. Am. Coll. Cardiol.* 2014; **63**:1145–1155, .
19. Papafaklis M, Muramatsu T, Ishibashi Y, Lakkas L, Nakatani S, Bourantas C, et al. Fast virtual functional assessment of intermediate coronary lesions using routine angiographic data and blood flow simulation in humans: comparison with pressure wire fractional flow reserve. *EuroIntervention* 2014; **10**:574–583, .

20. Tu S, Barbato E, Köoszegi Z, Yang J, Sun Z, Holm N, et al. Fractional flow reserve calculation from 3-dimensional quantitative coronary angiography and TIMI frame count: a fast computer model to quantify the functional significance of moderately obstructed coronary arteries. *JACC Cardiovasc. Interv.* 2014; **7**:768–777, .
21. Zhang JM, Zhong L, Luo T, Lomarda A, Huo Y, Yap J, et al. Simplified models of non-invasive fractional flow reserve based on CT images. *PLoS ONE* 2016; **11**(5):e0153 070, .
22. Shi C, Zhang D, Cao K, Zhang T, Luo L, Liu X, Zhang H. A study of noninvasive fractional flow reserve derived from a simplified method based on coronary computed tomography angiography in suspected coronary artery disease. *Biomed. Eng. Online* 2017; **16**:43, .
23. Bessems D. On the propagation of pressure and flow waves through the patient-specific arterial system. Ph.D. Thesis, TU Eindhoven, The Netherlands 2007.
24. Renker M, Schoepf U, R W, Meinel F, Rier J, Bayer R, et al. Comparison of diagnostic value of a novel noninvasive coronary computed tomography angiography method versus standard coronary angiography for assessing fractional flow reserve. *Am. J. Cardiol.* 2014; **114**:1303–1308, .
25. Boileau E, Nithiarasu P. One-dimensional modelling of the coronary circulation. Application to noninvasive quantification of fractional flow reserve (FFR). *Computational and Experimental Biomedical Sciences: Methods and Applications*, *LN Comput. Vis. Biomech.*, vol. 21, Tavares J, Jorge R (eds.). Springer International, 2015; 137–155.
26. Baumann S, Wang R, Schoepf U, Steinberg D, Spearman J, Bayer R, et al. Coronary CT angiography-derived fractional flow reserve correlated with invasive fractional flow reserve measurements–initial experience with a novel physician-driven algorithm. *Eur. Radiol.* 25; **2015**:1201–2017, .
27. Coenen A, Lubbers M, Kurata A, Kono A, Dedic A, Chelu R, et al. Fractional flow reserve computed from noninvasive CT angiography data: diagnostic performance of an on-site clinician-operated computational fluid dynamics algorithm. *Radiology* 2015; **274**:674–683, .
28. Wang R, Renker M, Schoepf U, Wichmann J, Fuller S, Rier J, et al. Diagnostic value of quantitative stenosis predictors with coronary CT angiography compared to invasive fractional flow reserve. *Eur. J. Radiol.* 2015; **84**:1509–1515, .
29. Itu L, Rapaka S, Passerini T, Georgescu B, Schwemmer C, Schoebinger M, et al. A machine-learning approach for computation of fractional flow reserve from coronary computed tomography. *J. Appl. Physiol.* 2016; **121**:42–52, .
30. Tröbs M, Achenbach S, Röther J, Redel T, Scheuering M, Winneberger D, et al. Comparison of fractional flow reserve based on computational fluid dynamics modeling using coronary angiographic vessel morphology versus invasively measured fractional flow reserve. *Am. J. Cardiol.* 2016; **117**:29–35, .
31. Ko B, Cameron J, Munnur R, Wong D, Fujisawa Y, Sakaguchi T, et al. Noninvasive CT-derived FFR based on structural and fluid analysis: A comparison with invasive FFR for detection of functionally significant stenosis. *JACC Cardiovasc. Imaging* 2016; .
32. Wilson R, Wyche K, Christensen B, Zimmer S, Laxson D. Effects of adenosine on human coronary arterial circulation. *Circulation* 1990; **82**:1595–1606, .
33. Mantero S, Pietrabissa R, Fumero R. The coronary bed and its role in the cardiovascular system: a review and an introductory single-branch model. *J. Biomed. Eng.* 1992; **14**:109–116.
34. West G, Brown J, Enquist B. A general model for the origin of allometric scaling laws in biology. *Science* 1997; **276**:122–126.
35. Kim H, Vignon-Clementel I, Coogan J, Figueroa C, Jansen K, Taylor C. Patient-specific modeling of blood flow and pressure in human coronary arteries. *Ann. Biomed. Eng.* 2010; **38**:3195–3209, .
36. Taylor C, Fonte T, Min J, City R, Angeles L. Computational fluid dynamics applied to cardiac computed tomography for noninvasive quantification of fractional flow reserve: scientific basis. *J. Am. Coll. Cardiol.* 2013; **61**:2233–2241, .

37. Aarnoudse W, Fearon W, Manoharan G, Geven M, Van De Vosse F, Rutten M, et al. Epicardial stenosis severity does not affect minimal microcirculatory resistance. *Circulation* 2004; **110**:2137–2142, .
38. Antiga L, Piccinelli M, Botti L, Ene-Iordache B, Remuzzi A, Steinman D. An image-based modeling framework for patient-specific computational hemodynamics. *Med. Biol. Eng. Comput.* 2008; **46**:1097–1112, .
39. Choy J, Kassab G. Scaling of myocardial mass to flow and morphometry of coronary arteries. *J. Appl. Physiol.* 2008; **104**:1281–1286, .
40. Spaan J. Coronary diastolic pressure-flow relation and zero flow pressure explained on the basis of intramyocardial compliance. *Circ. Res.* 1985; **56**:293–309.
41. Bruinsma P, Arts T, Dankelman J, Spaan J. Model of the coronary circulation based on pressure dependence of coronary resistance and compliance. *Basic Res. Cardiol.* 1988; **83**:510–524.
42. Spaan J, Cornelissen A, Chan C, Dankelman J, Yin F. Dynamics of flow, resistance, and intramural vascular volume in canine coronary circulation. *Am. J. Physiol. Heart Circ. Physiol.* 2000; **278**:H383–H403.
43. Cain P, Ahl R, Hedstrom E, Ugander M, Allansdotter-Johnsson A, Friberg P, Arheden H. Age and gender specific normal values of left ventricular mass, volume and function for gradient echo magnetic resonance imaging: a cross sectional study. *BMC Med. Imaging* 2009; **9**(2), .
44. Mynard J, Penny D, Smolich J. Scalability and in vivo validation of a multiscale numerical model of the left coronary circulation. *Am. J. Physiol. Heart Circ. Physiol.* 2014; **306**:H517–528, .
45. Smith N, Pullan A, Hunter P. An anatomically based model of transient coronary blood flow in the heart. *SIAM J. Appl. Math.* 2002; **62**:990–1018.
46. Boileau E, Nithiarasu P, Blanco P, Müller L, Fossan F, Hellevik L, et al. A benchmark study of numerical schemes for one-dimensional arterial blood flow modelling. *Int. J. Numer. Method Biomed. Eng.* 2015; **31**, .
47. Olufsen M. Structured tree outflow condition for blood flow in larger systemic arteries. *Am. J. Physiol.* 1999; **276**:H257–H268.
48. Taylor CA, Hughes TJ, Zarins CK. Finite element modeling of blood flow in arteries. *Computer methods in applied mechanics and engineering* 1998; **158**(1-2):155–196.
49. Updegrove A, Wilson NM, Merkow J, Lan H, Marsden AL, Shadden SC. Simvascular: An open source pipeline for cardiovascular simulation. *Annals of Biomedical Engineering* 2016; :1–17.
50. Moghadam ME, Vignon-Clementel IE, Figliola R, Marsden AL, of Congenital Hearts Alliance (mocha) Investigators M, *et al.*. A modular numerical method for implicit 0d/3d coupling in cardiovascular finite element simulations. *Journal of Computational Physics* 2013; **244**:63–79.
51. De Bruyne B, Pijls N, Heyndrickx G, Hodeige D, Kirkeeide R, Gould K. Pressure-derived fractional flow reserve to assess serial epicardial stenoses: Theoretical basis and animal validation. *Circulation* 2000; **101**:1840–1847, .
52. Iguchi T, Hasegawa T, Nishimura S, Nakata S, Kataoka T, Ehara S, et al. Impact of lesion length on functional significance in intermediate coronary lesions. *Clin. Cardiol.* 2013; **36**:172–177, .
53. Singla S, Sachdeva R, Uretsky B. Normal fractional flow reserve with a critical stenosis supplying viable myocardium. *Exp. Clin. Cardiol.* 2012; **17**:142–143.
54. McGinn A, White C, Wilson R. Interstudy variability of coronary flow reserve. Influence of heart rate, arterial pressure, and ventricular preload. *Circulation* 1990; **81**:1319–1330.
55. Jeremias A, Filardo S, Whitbourn R, Kernoff R, Yeung A, Fitzgerald P, Yock P. Effects of intravenous and intracoronary adenosine 5'-triphosphate as compared with adenosine on coronary flow and pressure dynamics. *Circulation* 2000; **101**:318–323.